Measurement of Brownian motion of nanoparticles in suspension using a network-based PTV technique

A. Banerjee, C. K. Choi and K. D. Kihm

Mechanical, Aerospace and Biomedical Engineering Department
University of Tennessee, Knoxville, TN 37996
E-mail: kkihm@urk.edu, Homepage: http://go.to/microlab

T. Takagi

Department of Electrical Engineering
Kushiro National College of Technology, Kushiro, Japan

Abstract: A comprehensive three-dimensional nano-particle tracking technique in micro- and nano-scale spatial resolution using the *Total Internal Reflection Fluorescence Microscope* (TIRFM) is discussed. Evanescent waves from the total internal reflection of a 488nm argon-ion laser are used to measure the hindered Brownian diffusion within few hundred nanometers of a glass-water interface. 200-nm fluorescence-coated polystyrene spheres are used as tracers to achieve three-dimensional tracking within the near-wall penetration depth. A novel ratiometric imaging technique coupled with a neural network model is used to tag and track the tracer particles. This technique allows for the determination of the relative depth wise locations of the particles. This analysis, to our knowledge is the first such three-dimensional ratiometric nano-particle tracking velocimetry technique to be applied for measuring Brownian diffusion close to the wall.

Keywords: Nano-Particle, TIRFM, Brownian diffusion, Neural Network, 3D Tracking

1. Introduction

Single molecule detection techniques (SMD) to visualize the dynamic behavior and reaction kinetics of individual molecules in living cells have recently attracted a great deal of attention (Xie, 2001 and Weiss, 2000). The rapid development and progress of SMD techniques have ushered in a revolution in biological research. It is known that the reaction of biological molecules is generally stochastic. Thus, even if the reactions of bio-molecules are initiated at the same time, they cannot be synchronized as a result of which dynamic behaviors of individual molecules are averaged and hidden in the ensemble-averaged movements (Ishijima and Yanagida, 2001). SMD is generally based on two key technologies, single molecule imaging and single molecule manipulation. But there are certain optical issues associated with the detection and subsequent tracking of single molecules. The size of individual molecules is on the order of nano-meters and so they are too small to be visualized by conventional optical microscopy. To overcome this problem, bio-molecules are labeled and visualized using fluorescence microscopy.

Fluorescence microscopy has been an extremely powerful tool for biologists to study various

characteristics of living cells over the last few decades. The non-invasive nature of the fluorophores associated with the high sensitivity and contrast has made fluorescence microscopy a prominent tool in modern cell biology (Lange et al, 2001). Moreover the very nature of light allows different contrast mechanisms like polarization and phase discrimination that yields additional information. However, a significant drawback of light microscopy is dictated by the laws of diffraction. The limit of resolution that can be reached by optical techniques is directly proportional to the wavelength of incident light (Hecht, 2002). This diffraction limit originates from the fact that it is impossible to focus a beam of light to a spot smaller than its wavelength. The challenge to break this diffraction limit has led to the development of several novel imaging techniques. One of them, Total Internal Reflection Fluorescence Microscopy (TIRFM) uses an electromagnetic field called the 'evanescent field' to excite the fluorophores within one to several hundred nanometers from the interface (Axelrod et al, 1992). Because any background fluorescence is excited, this method provides a significant improvement for near field illumination compared to differential interference contrast (Inoue, 1987), confocal microscopy (Pawley, 1995), theta microscopy (Stelzer and Lindek, 1994) or multi-photon microscopy (Denk et al., 1990). Additionally all these methods are limited in spatial resolution (Rohrbach, 2000).

TIRFM has been a very popular technique for both in vitro and in vivo single molecule detection (Ishijima and Yanagida, 2001 and Sako et al, 2000). Originally developed to study the interface phenomenon between two media of different refractive indices, the fundamental concept of TIRFM is simple requiring only an excitation light beam traveling at a high incident angle from the denser medium to the rarer medium (Axelrod et al, 1984). Differences in refractive index between the denser (glass cover slip) and rarer (aqueous) medium regulate how light is refracted or reflected at the interface as a function of incident angle. At an angle greater than the critical angle, rather than passing through and refracting in accordance with Snell's Law, the beam of light is totally reflected from the glass/water interface (Hecht, 2002). This total reflection generates a very thin electromagnetic field (usually less than 200 nanometers) in the aqueous medium, which has an identical frequency to that of the incident light (Goos-Hanchen Effect). This leakage popularly called the evanescent wave or field undergoes exponential intensity decay with increasing distance from the surface (Hecht, 2002, and Born and Wolf, 1980). Using such a narrow excitation depth is the most effective way to overcome the background noise problem which is often the biggest problem in single molecule imaging (Sako and Yanigida, 2003). Previously, TIRFM was difficult to perform because of the complexity of the microscope set up and the problem of achieving acceptable image brightness. But with the advent of new high Numerical Aperture (NA) lens (NA greater than 1.4) and fast frame rate sensitive cameras, the above complexities have been reduced greatly and the method is gaining popularity in a wide variety of applications.

Over the last decade, there has been significant development in production of miniaturized devices with advent of micro- and nano-technology. Usage of these devices for medical applications like drug delivery require the proper understanding of diagnostic techniques for measuring the velocity and concentration fields of fluid flow in these devices. Micron order - Particle imaging velocimetry (μ-PIV) using a fluorescence microscope has been developed successfully and has become a useful technique for measuring velocity fields in micro-devices (Santiago et al 1998). The major sources of error in these techniques arise from the variations in particle velocity over the out-of-plane spatial resolution, high background noise, and a diffraction-limited spot size. A series of theoretical and experimental studies was performed to alleviate the optical difficulties and improve the particle visibility (Olsen and Adrian 2000 and Meinhart et al 2000). However, all these systems have a spatial resolution in the order of microns and it is not possible to measure near wall flow characteristics with these systems. Very recently, new diagnostic techniques capable of approaching sub-micron or nano-meter length scales near a wall using TIRFM have been proposed (Zettner and Yoda, 2003 and Jin et al, 2003). However, these studies are two dimensional in nature and suffer from out of plane spatial resolution and errors resulting from particle dropout due to out of plane motion (Zettner and Yoda, 2003). Furthermore it has been found that the dynamics of the particles close to the wall become significantly non-Gaussian and the average particle displacement differs from the theoretical most probable particle displacement (Jin et al, 2003). Thus it becomes essential to analyze the out of plane velocity components and the non-Gaussian behavior of the particle displacement.

The current paper talks about a novel three dimensional particle tracking velocimetry technique (Banerjee *et al.* 2003) using variable angle ratiometric TIRFM Imaging. By varying the incident angle of the laser beam, evanescent waves of varying penetration depths were generated. By measuring the fluorescence intensity of the individual molecules at these depths, a three dimensional reconstruction of the particle position is performed (Rohrbach *et al.,* 2000). Single Particle tracking using a novel Neural Network Model reveals a phenomenon of hindered diffusion near a wall. The results are compared with a corrected Stokes flow model (Goldman et al., 1967 and Brenner, 1961). This study is also the first attempt to experimentally validate the phenomenon of hindered diffusion near wall in micro-fluidic devices, thereby considerably improving upon the previous TIRFM experiments.

2. Evanescent Wave Theory & TIRFM System

2.1 Evanescent Wave Theory

Light beam propagating through a medium having a high refractive index (n_i) is refracted according to Snell's Law when it encounters a boundary to a medium of lower refractive index (n_t). As the incident angle slowly increases (relative to the normal), it reaches a point where the angle of refraction is 90°. This angle of incidence is commonly known as the *critical angle:* $\theta_c = \sin^{-1}(n_t / n_i)$.

At angles larger than the critical angle, light is completely reflected at the interface (total internal reflection), and no significant amount is refracted into the bulk phase of the rarer medium. However a small portion of the reflected light penetrates through the interface, and propagates parallel to the surface in the plane of incidence creating an electromagnetic field in the liquid adjacent to the interface. This field, termed as the *evanescent field* is capable of exciting fluorophores residing in the immediate region near the interface. The evanescent wave penetrates into the less dense medium and propagates parallel to the interface with an intensity I that decays exponentially with normal distance z away from the interface located at $z = 0$.

$$I(z) = I_0 \exp\left(-\frac{z}{z_p}\right) \tag{1}$$

where I_0 is the light intensity at the interface and z_p is the penetration depth of the wave. The penetration depth is dependent on the wavelength (λ_0) of incident light beam in vacuum (I_0) and the refractive indices of the medium under consideration (n_i, n_t) as can be seen from Eq.(2).

$$z_p = \frac{\lambda_0}{4\pi}\left(n_i^2 \sin^2 \theta - n_t^2\right)^{-\frac{1}{2}} \tag{2}$$

In general, the value of z_p is on the order of the incident wavelength, or perhaps somewhat smaller. When the incident angle equals the critical value, z_p goes to infinity, and the wave fronts of refracted light are normal to the surface. For the wavelength range 472-532 nm (blue-green band), the value of penetration depth is in the order of a few hundred nanometers.

Traditionally, two different configurations of TIRFM are popular. The first set up with a prism can be easily achieved and requires only the microscope, prism, and laser and all these are components that are readily available. The main drawback for this setup is the requirement that the specimen be positioned between the prism and the microscope objective. The second setup requires that the laser be introduced through the microscope, and greatly benefits from an objective lens with a numerical aperture (NA) greater than 1.4.The specimen must be located on the bottom surface of the cover glass. The preparation, facing away from the objective, is accessible and permits the use of other instrumentation such as micromanipulator, differential interference contrast (DIC) illuminating optics and a scanning probe microscope.

2.2 High NA Objective based TIRFM System

An Olympus Plan APO 60X oil immersed TIRF lens with a NA of 1.45 has been used for performing

TIRFM experiments. The experimental setup consists of an inverted microscope (IX-50, Olympus, Japan), a 200-mW CW argon-ion laser (tuned at 488-nm, Laser Physics, U.S.A.); a frame grabber board (QED Imaging, U.S.A.), and PTV analysis software. The upper outlet port of the IX50 is connected to the CCD camera (UP-1830 UNIQ, 1024 × 1024 pixels at 30 frames per second). A stack of 90 images is saved for each run and the frames are analyzed. Seeding particles used are yellow-green (excitation peak at 505 nm and emission peak at 515 nm) biotin coated fluorescent micro-sphere beads of 200-nm diameter which have a specific gravity of 1.05 (Molecular Probes, U.S.A.). The experimental set up is illustrated in Fig. 1.

The optical set up is complex as light needs to pass through the very perimeter of the 60X NA 1.45 (n=1.515) oil immersed objective lens. The critical angle for the lens with total internal reflection at a water-glass interface is $\sin^{-1}(1.33/1.515) = 61.38°$. For a NA of 1.45, the maximum angle of passage of light is $\sin^{-1}(1.45/1.515) = 73.15°$. Thus the angle available for Total Internal Reflection and changing the depth of field of the evanescent wave is $(73.15° - 61.38°=)$ 11.77°. The incident angles for the experiment were varied between 62° $(z_p = 245$ nm$)$ to 68° $(z_p = 86$ nm$)$.

3. Ratiometric Imaging

3.1 Theory of Ratiometric Imaging

The aim of the detection technique is to generate and measure an exponentially decaying intensity volume within which the detection will take place. For a homogeneous medium, this detection volume is defined by the point spread function $PSF(z)$ of the microscope objective. The point spread function has a finite depth of focus (in the z direction) and a defined volume. Because of refractive index mismatch (between glass and water), the optical path lengths of light are significantly altered. As a result, an increase of PSF by ~ 10% has been found in both lateral and axial directions (Rohrbach, 2000). The presence of a dielectric interface (the coverslip in this case) significantly alters the probability of detecting the emitted fluorophores. This effect is traditionally defined by the collection efficiency Q (z) of the objective lens. The collection efficiency is defined as the collected power to the total power dissipated by a dipole. Detailed mathematical formulations of Q (z) have been attempted by various authors (Burghardt and Thompson, 1984; Hellen and Axelrod, 1986).

The fluorescence $F(x,y;z_p)$ detected by a microscope objective is modeled as a function of the 3-dimensional fluorophore distribution $C(x,y,z)$. For any pixel (x,y), the detected signal can be described by

$$F(x,y;z_p) = \varepsilon \cdot I_0(x,y;z_p) \cdot \int_0^\infty [Q(Z) \cdot PSF(z)] \cdot C(x,y,z)e^{-\frac{z}{z_p}} dz \qquad (3)$$

where ε defines the quantum efficiency of fluorescent particles and of the CCD camera and I_0 $(x,y;z_p)$ is the light intensity at the interface. The integration in the axial (z) direction is done by the microscope objective so that $F(x,y;z_p)$ is measured by the CCD camera. The quantum efficiency ε is assumed to be equal for all penetration depths and is set equal to 1. The PSF (z) for the experimental configuration is nearly constant for the extension of the evanescent wave is set equal to 1. The incident intensity on the glass-water interface is difficult to measure as it passes through a series of lenses as illustrated in Fig. 1. Therefore $I_0(x,y;z_p)$ and the $C(x,y,z)$ are the only two unknown parameters in Eq. (3) . Thus Eq. (3) in normalized by dividing by the $I_0(x,y;z_p)$ to obtain intensity per pixel $I(x,y;z_p)$.

$$I(x,y;z_p) = \frac{F(x,y;z_p)}{I_0(x,y;z_p)} = \int_0^\infty C(x,y,z) \cdot Q(z) \cdot e^{-\frac{z}{z_p}} dz \qquad (4)$$

The function $C(x,y,z)$ can be described in terms of the radius R of the sphere , the fluorophore amount c inside the sphere and the separation distance h to the interface as shown in Fig. 2. Thus

the fluorophore distribution is defined as follows:

$$C(x,y,z) = c \quad \text{if} \quad \sqrt{x^2 + y^2 + (z-h)^2} \leq R$$
$$= 0 \quad \text{if} \quad \sqrt{x^2 + y^2 + (z-h)^2} > R \tag{5}$$

The fluorescence is detected and integrated over the whole spherical volume with the assumption that the excitation field intensity inside the sphere is equal to the incoming light field Intensity (First Born Approximation).Thus for a constant collection efficiency of $Q(z)=1.0$, after integrating over (x,y), we define $I_N(a,R,c) = \iint I(x,y;z_p)dxdy$. The integral in Eq. (3) when converted to cylindrical co-ordinates reduces to

$$I_N(a,R,c) = c \cdot 2\pi \cdot \int_0^{\sqrt{R^2-z^2}+R} \int_{-R}^{z+h} Q(z) \cdot e^{-\frac{z+h}{z_p}} r \, dr \, dz$$

$$= 4\pi \, c \, z_p^3 \left[\left(\frac{R}{z_p} \right) \cosh\left(\frac{R}{z_p} \right) - \sinh\left(\frac{R}{z_p} \right) \right] \cdot e^{-\frac{h}{z_p}} \tag{6}$$

Thus Eq. (6) gives a value of the normalized intensity per pixel in terms of the geometrical parameters h and R as well as the evanescent field depth z_p. However c is difficult to measure and not accurately known. So to evaluate the elevation h of the particle above the interface, particle pairs particle pairs were identified. By taking a ratio of the pixel intensity values for a pair of particles on an image, the relative axial (z) position Δh of the particles in the image was evaluated as shown in Eq. (7)

$$\frac{I_N^1(a,R,c)}{I_N^2(a,R,c)} = \exp\left(-\frac{\Delta h}{z_p} \right) \tag{7}$$

Equation (7) gives a relative depth wise location Δh of various particles. To obtain the absolute position of the particles, care is taken to focus at a particle which is immobile and at the glass-water interface. This particle is found to have the maximum pixel intensity. Thus by default, the brightest particle is at the interface corresponding to an axial location of $z = 0$. The intensity of other particles in the image is identified and the ratiometric technique is utilized to evaluate the absolute depths (h) of the particles from the interface.

3.2 Measurement Uncertainty in Ratiometric Imaging

However measurement of I_N as per equation 6 involves a number of errors because of background noise in the image. The various errors may be attributed to background fluorescence (ΔI_F), photon noise (ΔI_{PN}), errors in surface intensity (ΔI_o) and errors associated with the lateral scattering of excitation light (ΔI_S). The strongest disturbance ΔI_S is eliminated by using a low mass per unit volume ratio (0.001% by volume) of the fluorophore in water and keeping the penetration depths below 250 nm. Under these conditions, the background intensity can be estimated with a mean signal to noise ratio. The photon noise depends on the exposure time of the CCD camera and for the current experimental conditions it is less than 1%. The errors in surface intensity are taken as instrumental errors and it includes the uncertainty in the refractive indices of the cover glass and well as that of the fluorophore solution. A Gaussian 5×5 filter is used to eliminate the background noise. It should be noted that for the overall uncertainty, the maximum error is associated with the mean error in the granule diameter for the fluorophores. The total error associated with all these terms are incorporated in the final uncertainty analysis and an estimation of the overall uncertainty is provided. A Kline McClintock uncertainty analysis is performed on equations 2 and 6 to find the overall uncertainty of the measured intensities and the separation distances. A maximum uncertainty of 1% was observed for the pixel intensities whereas the separation distances had an uncertainty of 2%.

4. Discussions

4.1 A Discussion on Brownian Motion

The observation of random motion was first reported by Jan Ingenhousz in 1785 and was subsequently rediscovered and named after Brown in 1828. Albert Einstein used the kinetic theory to derive the diffusion constant for such motion in terms of fundamental parameters of the particles and liquid. The mathematics of Brownian motion is actually deep and subtle. Various authors have erred in defining a constant velocity v for Brownian trajectory by taking the limit $\Delta x / \Delta t$ for small displacement Δx and small time Δt. The proper limit involves forming the diffusion coefficient $D = (\Delta x)^2 / \Delta t$ as both Δx and Δt go to zero. In other words, since the random walk displacement in Brownian motion grows only as the square root of time, velocity scales like $\Delta t^{-1/2}$ and is therefore not defined in the small Δt limit. Thus for a given time interval, the parameter to be used for defining a random walk pattern is the mean square displacement (MSD). A three dimensional MSD $\langle r \rangle^2$ defined by the Einstein-Smoluchowski Equation is given as follows:

$$\langle r \rangle^2 = \langle x \rangle^2 + \langle y \rangle^2 + \langle z \rangle^2 = 6D\Delta t \tag{8}$$

where D is the diffusion coefficient defined by Einstein in 1905 (also published in 1907) and is given as follows:

$$D = \frac{kT}{3\pi\mu d_p} \tag{9}$$

In Eq. (9), k is Boltzman's constant, T is the absolute temperature and μ is the dynamic viscosity of the fluid. Thus for analysis of a two dimensional mean square distance of diffusion (which is utilized for measuring the tangential diffusion coefficient), the Einstein-Smoluchowski Equation reduces to:

$$\langle r \rangle^2 = \langle x \rangle^2 + \langle y \rangle^2 = 4D\Delta t \tag{10}$$

The MSD of the particles in evaluated by calculating mean of the square displacements of all particle on the image plane: $\langle r \rangle^2 = \sum_i^n r_i^2 \Big/ n$. But, the mean displacement is not simply a square root of this value and is given by $\langle r \rangle = \sum_i^n r_i \Big/ n$. Therefore the Brownian velocity should not be erroneously defined as $v_B = \sqrt{\langle r \rangle^2 / \Delta t}$. A standard error can be calculated based on MSD which gives the lower limit of the time interval Δt.

4.2 The Phenomenology of Hindered Diffusion close to a wall

The chemical potential, η_i of the substance within a phase at equilibrium is constant in the absence of any external fields. If however, the value of η_i varies from place to place, then substance i will tend to diffuse is such a way as to equalize the values throughout the phase. The driving force F_d for this diffusion process is the spatial gradient of η_i and can be written as:

$$F_d = -\nabla \eta_i \tag{11}$$

There is, on average, no actual force on the molecules or particles of i since they move only to maximize the entropy of the system. However the introduction of this pseudo-force aids the analysis. The chemical potential can be defined in terms of concentration c_i as:

$$\eta_i = \eta_i^0 + RT \ln c_i \tag{12}$$

Since η_i^0 is constant throughout the phase, we can write equation 11 as:

$$F_d = -\frac{RT}{c_i}\nabla c_i \tag{13}$$

This force acting on the particle sets it in motion; it will be opposed by a viscous drag force, F_d, which for a particle of reasonably smooth shape is proportional to its velocity and is known as Stokes Law. As the particle increases in velocity, F_d increases until it equals the diffusion force and the particle then reaches its terminal velocity. We then have:

$$F_d = 3\pi\mu d_p u_d \tag{14}$$

However, Stokes Law applies only to a fluid media that extend to infinity in all directions. In most cases however, this assumptions does not strictly hold true as a free surface or a rigid wall forms an externally bound to the fluid. The presence of these boundaries at finite distances from the particle necessitates the corrections to the Stokes' resistance formula. Brenner (1961) provided an analytical expression in form of an infinite series for this correction term. He used a hypothesis of no relative motion at the fluid solid interface. Thus if ξ is the correction which must be applied to Stokes' Law as a result of the presence of the solid wall, then:

$$F_d = 3\pi\mu d_p u_d \xi^{-1} \tag{14'}$$

where:
$$\xi^{-1} = \frac{4}{3}\sinh\alpha \cdot \sum_{n=1}^{\infty}\frac{n(n+1)}{(2n-1)(2n+3)}\left[\frac{2\sinh(2n+1)\alpha+(2n+1)\sinh 2\alpha}{4\sinh^2(n+\frac{1}{2})\alpha+(2n+1)^2\sinh^2\alpha}-1\right] \tag{15}$$

The parameter α in Eq. (15) is a function of the particle diameter d_p and the elevation h from the interface to the base of the sphere.

$$\alpha = \cosh^{-1}\left(\frac{2h+d_p}{d_p}\right) \tag{16}$$

The diffusion velocity u_d is related to the flux of material per unit area, J_i by:

$$J_i = u_d c_i \tag{18}$$

The flux J_i is connected to the diffusion coefficient D by Fick's First Law of Diffusion:

$$J_i = -D\nabla c_i \tag{19}$$

Thus by solving equations 9-19, we get the "hindered" normal diffusion coefficient D_{normal} of a spherical particle at a distance h from the wall as:

$$D_{normal} = \xi\frac{kT}{3\pi\mu d_p} = \xi \cdot D \tag{20}$$

Equation (20) gives an estimate of the one dimensional normal hindered diffusion at a height h from the wall. This quenching of diffusion can be attributed more in the normal z-direction and less in the tangential x-y plane. This claim is validated by the work of Goldman et al. (1967) which analyzes the slow viscous motion of the sphere parallel to a plane wall bounding a semi-infinite, quiescent and viscous fluid. An asymptotic solution of Stokes Equation leads to a value of the corrected tangential force and torques on the spherical particle. Thus if β is the correction which must be applied to the tangential force as a result of the presence of the solid wall, we have

$$F_d = 3\pi\mu d_p u_d \beta^{-1} \tag{21}$$

where:
$$\beta = \left[1 - \frac{9}{16}\left(\frac{d_p}{d_p + 2h}\right) + \frac{1}{8}\left(\frac{d_p}{d_p + 2h}\right)^3 - \frac{45}{256}\left(\frac{d_p}{d_p + 2h}\right)^4 - \frac{1}{16}\left(\frac{d_p}{d_p + 2h}\right)^5 \right] \tag{22}$$

Equation (22) is a function of the particle diameter d_p and its elevation from the interface h. Thus by similarly solving equations 9-22, we get the "hindered" tangential diffusion coefficient $D_{tangentail}$ of a spherical particle at a distance h from the wall as:

$$D_{\tan gential} = \beta D \tag{23}$$

However, since the particle tracking is in three dimensions, it becomes important to define a bulk hindered diffusion coefficient. Keeping in mind that Einstein-Smoluchowski Equation gives: $\langle x^2 \rangle = \langle y^2 \rangle = \langle z^2 \rangle = 2Dt$. So using Eqns. (8), (20) and (23), we get the correction factor for the bulk three dimensional diffusion co-efficient as:

$$\psi = \frac{2\beta + \xi}{3} \tag{24}$$

The values of ξ, β and ψ for a particle diameter of 200nm and for various elevations from the base of the sphere, are tabulated in Fig. 3. It should be noted that the above analysis is approximate in nature as it talks about the interaction of a single particle with wall. In reality, multiple particles are present and care should be exercised to take into consideration the hydrodynamics of all the particles in the image plane. However, if the ratio of the particle radii to the separation distance is great than 10, effects between particles can be neglected. Particle-particle interaction is kept to a minimum in the experiment by taking a volume fraction of 0.001%.

5. Results and Discussion

5.1 Transient Velocity Tracking

Figure 4 provides a comparison between the direct and the evanescent illumination. Light scattering from out of focus particles causes significant background noise. The signal to noise ratio (SNR) for such case is low. It can be seen that for a TIRFM Image, the thin penetration depth of an evanescent wave reduces the background noise. As the angle of incidence is increased from 62° to an angle of 68°, the penetration depth (z_p) of the wave reduces from 272 nm to 85 nm. Thus it can be observed from Fig. 4(b)- 4(d) that the SNR increases for a higher angle of incidence giving a stronger signal. Since an angle of 68° provides a higher SNR value, all subsequent analysis is done on these data.

For each angle a set of 90 images in a stack is captured. Figure 5 provides the axial (z) locations of the particles for frame 33 when the angle of incidence is 68°. When the experiments are performed, care is taken to focus at a particle which is immobile and at the glass-water interface. This particle is found to have the maximum pixel intensity. Thus by default, the brightest particle is at the interface corresponding to an axial location of $z = 0$. The intensity of other particles in the image is identified and the ratiometric technique is utilized to evaluate the relative depths (Δd) of the particles from the interface. The particles are tagged in figure 5 to illustrate this principle. It is worth mentioning here that a microscope 2-D image actually contains 3-D information. This simple ratiometric technique provides a faster deconvolution procedure and also possesses higher spatial resolution than standard deconvolution or confocal techniques.

Particle # 6 is chosen at random from the tagged particles and the axial as well as the lateral positions of the particle is tracked. The particle illustrates a random Brownian diffusion and moves close to the wall as illustrated in figure 6. The evanescent field thickness for the case under consideration is 86 nm. As the distance of the particle from the interface increases, the intensity decreases exponentially and an upper limit of observation depth is needed to be established. The cut off amplitude for segmentation corresponding to 15% of the peak intensity is taken as this upper limit. Thus the particles are seen to be within 150 nm from the wall. There are instances when the particle moves away from the illumination field. For all such cases, the depth is

calculated from the cut off intensity and the particle position is tracked. Individual particles are tracked in three dimensions over 60 frames and the particle displacements are plotted in Figure 7. It is seen that the displacement is severely hindered in the direction normal to the interface as the z-displacements are an order smaller than the corresponding x and y displacements.

5.2 Neural Network based 3D PTV

The novel neural network model finds the relationship among particles between a pair of images (Takagi and Okamoto, 2001). A simple two-layered network is chosen for analysis. The first layer of the network is the input layer that corresponds to the ith image. The second layer corresponds to the $(i+1)^{th}$ image. All interconnections go from the first layer to the second layer and the two layers are fully interconnected as seen in Fig. 8a. To correspond between particles of the first and the second layers, sets of the particle labels of each image are assumed to be $P = \{p_1, p_2, \cdots, p_n\}$ and $Q = \{q_1, q_2, \ldots, q_n\}$. The coordinates corresponding to the label of each particle in first layer is (x_{pn}, y_{pn}) while in second layer it is given by (x_{qn}, y_{qn}). The distance function between particles of the two successive layers is as follows:

$$d_{i,j} = \left(x_{p,i} - x_{q,j}\right)^2 + \left(y_{p,i} - y_{q,j}\right)^2 \tag{25}$$

The overall operation of the network model is similar to the competitive learning paradigm (Kohonen et al., 1994). However, the network model differs in the details of its equations and the weights to update on training cycle. Each interconnection in the network model has an associated weight value (Kohonen, 1995). The initial state of the network has small values for the weights. The weight values are a rate of the correspondence level. Then, the initial weight values are set by the average value of a rate of the correspondence level. The weight values are updated during the training of the network. Figure 8b illustrates architecture of the network model.

The network model uses interconnected fully between particles can be composed on the network (Okamoto et al., 1995 and 1997). A basic structure of the network model is two-layered network that consists of the first image and the second image. The particle of the first image is connected with the weight in all particles of the second images in Fig. 8b. The next equation is an update rule of the weight of the network model in this technique.

$$w_{,j}(t+1) = w_{i,j}(t) - \alpha \cdot d_{i,j} \cdot w_{i,j}(t) \tag{26}$$

where, weight $w_{ij}(t)$ is the value of a weight from particle i of the first image to particle j of the second image prior to adjustment. $w_{ij}(t+1)$ is the value of a weight from particle of i of the first image to particle j of the second image after adjustment. α, the momentum coefficient is set to $(0,1)$.

The value by which the distance between the particle position and the second image of the first image is regularized is assumed to be an initial value about the weights at the first stage. The weight is updated in proportion to the distance between particles by the update rule shown in Eq. (26). Next, the weight shown in Eq. (27) is regularized.

$$w'_{i,j} = \frac{w_{i,j}}{\sum\limits_{j=1}^{N} w_{i,j}} \tag{27}$$

The regularization of Eq. (26) shows the ratio of adoption degree with the particle of the second image to one particle with the first image. N shows the total of the particle of the second image. When the value of the weight between particles is large, the probability as the corresponding particle is high.

5.3 Processing and Diagnostics: Image processing for PTV

Figure9 gives the flow chart for the image processing algorithm that estimates the particle location for a chosen image and tracks the particle movement over a stack of images. The particle position

(x- and y-coordinates) is obtained from the center of the particle image as shown in Fig. 9. However, as already discussed, there is a significant background noise image. So as a first step, this noise is removed by using a standard 5×5 Gauss filter. Figure 10 shows the detected particle image before and after filtering. The depth wise position (z coordinate) of the particle is obtained from the mean value of the brightness of each particle as seen in Equation 6. In order to apply PTV, it is necessary to measure the position of the particle relative to the interface.

The segmentation is performed with a dynamic gray threshold. The gray level histogram is used to separate the particles from the background. The particle image is made binary by using a pre-determined gray level threshold. It is found that the size and the number of particles depend on the threshold as a result of which it should be chosen very carefully. The threshold is set to cut off 1% of the pixels from the highest value of the histogram using a p-tile method since the size of the particle being imaged are known. The images are dynamically changed to stabilize the number of particles. In order to identify connected pixel regions that show one particle, connected components labeling scans the image and groups into pixel components based on pixel connectivity. The particle image of the gray level is converted into a binary image by the threshold and the particle image and the background are shown by 0 and 1 respectively.

The connected components labeling operator scans the image by moving along a row until it comes to a point r which is 1. When this is true, it examines the eight neighbors of r which encountered in the scan. The labeling of r occurs as follows:

If all 8 neighbors are 0, assign a new label to this point, ELSE

If only one neighbor has 1, assign its label to this point, ELSE

If one or more of the neighbors have 1 assign one of the labels to this point and make a note of the equivalences.

For a pixel r with the coordinates (x,y) the set of pixels examined are given by figure 4c. The center coordinates (xc_i, yc_j) of the particle labeled q are obtained from the center of gravity of the light intensity value of each particle.

$$xc_q = \frac{1}{N_q}\sum_{x_i \in S_q} x_i; \quad yc_q = \frac{1}{N_q}\sum_{y_j \in S_q} y_j; \quad N_q \leftarrow (x_i, y_j) \in S_q \quad (28)$$

where S_q and N_q shows a set of particle q and the number of pixels that compose the particle q. The detected particles are labeled by the number. Crosses are the center of the particle divided into the particle and background by threshold as in Fig. 11. The light intensity of particle q is given by the average of intensity

$$I_q = \frac{1}{N_q}\sum_{x_i, y_j \in S_q} I(x_i, y_j) \quad (29)$$

Histogram of x, y and z as well as x-y, y-z and z-x is provided. It shows that the diffusion is hindered severely in the direction normal to the interface.

The 3-D displacements obtained from PTV analysis are plotted in Figure 12. The displacement vectors were calculated from the displacement of the centers of the particles. The displacements were first evaluated for each consecutive frame as illustrated in Figure 6. The displacements were then used to evaluate the mean square particle displacement. Since there was no pressure gradient in the system, the movement of the particles may be attributed to Brownian diffusion which is easily validated by the random nature of the movement. However the Brownian diffusion is seen to be severely quenched as in evidence from the skewness of the histogram for the mean square displacement in Figure 13. Its is seen the histogram for the mean square displacement in the z-direction is severely quenched than in the x and y directions.

The experimental observations were analyzed by the PTV method described in section 5.0 and by a manual single particle tracking of 3 particles taken at random. The experimental results are compared with the theoretical results obtained at a mean temperature of 293K where the Boltzman's constant k is 1.38054×10^{-23}/ K and the viscosity of water is taken as 1.0074×10^{-3}

N.s/m^2 . The value of h for the theoretical calculation was taken as 86 nm which is the Evanescent wave depth for the used angle of incidence (68°). The theoretical diffusion coefficients obtained from equations 16 and 17 are compared with the experimental diffusion coefficient obtained from the particle tracking analysis. The results are shown in table 1. It is seen that both the two- and three-dimensional mean square displacements as well as the Diffusion coefficients are in good agreement with the theoretical predictions.

6. Conclusive Remarks

A three-dimensional ratiometric PTV technique has been developed and used for measuring the hindered Brownian diffusion for 200 nm particles within 250 nm of the glass plate. The spatial resolution of the velocity data is 146.77 μm × 146.77 μm × 250 nm. The out-of-plane spatial resolution is determined by the penetration depth (z_p) for the evanescent wave which was varied from 250 nm to 86 nm depending on the angle of incidence. A possible source of error is the scarcity of particles close to the wall. This error is tackled by introducing the Network Model for tracking particle pairs.

The technique is the first of its kind to tag and track nano-particles in 3 dimensions with nanometer spatial resolution and can be used to investigate flows close to the solid surface which is important for measuring slip velocities as well as thermophoresis measurements. It is also the first attempt of its kind in microfluidics to analyze the effect of hindered diffusion very close to the wall. The results are in good agreement with the corrected Stokes theoretical model.

References

Axelrod D; Hellen EH; Fulbright RM (1992) Total Internal reflection fluorescence. In: Topics in Fluorescence Spectroscopy: Principles and Applications, Vol.3: Biochemical Applications. J. Lakowicz, ed. Plenum Press, New York, 289-343.

Axelrod D; Burghardt TP; Thompson NL (1984) Total Internal reflection fluorescence (in biophysics). Annl Rev of Biophys. and Bioengg. 13: 247-268.

Banerjee A; Chon C; Kihm KD (2003) Nanoparticle tracking using TIRFM imaging. 2003 IMECE Photogallery.

Born M; Wolf E (1980) Principles of Optics, 6th edn. Cambridge University Press, Cambridge, pp. 47-51.

Brenner H (1967) The slow motion of a sphere through a viscous fluid towards a plane surface. Chem. Engg. Sci. 16: 242-251.

Burghart TP; Thompson NL (1984) Effects of planar dielectric interfaces on fluorescence emission and detection. Biophys. J. 46: 729-737.

Denk W; Strickler JH; Webb WW (1990) Two photon laser scanning fluorescence microscopy. Science 248: 73-76.

Goldman AJ; Cox RG; Brenner H; (1967) Slow viscous motion of a sphere parallel to a plane-I: Motion through a quiescent fluid. Chem. Engg. Sci. 22: 637-651.

Hecht E (2002) Optics, 4th edn. Addison Wesley, Reading, Mass., pp 124-127.

Hellen EH; Axelrod D (1986) Fluorescence emission at dielectric and metal film interfaces. J. Opt. Soc. Am. B. 4: 337-350.

Inoue S (1987) Video Microscopy. Plenum Press, NY.

Ishijima A; Yanagida T (2001) Single molecule nanobioscience. Trends in Biochem Sci 26: 438-444.

Jin S; Huang P; Park J; Yoo JY; Breuer KS (2003) Near-Surface Velocimetry using Evanescent Wave Illumination. Proceedings of IMECE 2003:55015.

Kohonen T; Kaski S; Lappalainen H (1994) Self-Organization formation of various invariant-features filters in the adaptive subspace SOM. Neural. Comp. 9:1321-44.

Kohonen T (1995) Self-Organizing Maps. Springer-Verlag: Berlin.

Lange FD; Cambi A; Huijbens R; Bakker BD; Rensen W; Parajo MG; Van Hulst N; Figor CG (2001) Cell Biology beyond the diffraction limit: near field scanning optical microscopy. J Cell Sci. 114: 4153- 4160.

Meinhart CD; Wereley ST; Gray MHB (2000) Volume illumination for two- dimensional particle image velocimetry. Meas. Sci. Technol. 11: 809-814

Olsen MG; Adrian RJ (2000) Out-of-focus effects on particle image visibility and correlation in microscopic particle image Velocimetry. Exp Fluids, Suppl.:S166-S174

Okamoto K; Hassan YA; Schmidl WD (1995) New tracking algorithm for particle image velocimetry. Exp. Fluids 19: 342.

Okamoto K; Nishio S; Kobayashi T; Saga T (1997) Standard images for particle imaging velocimetry, Proc. of The Second Int. Workshop on PIV-97-Fukui, Japan: 229-236.

Pawley JB (1995) Handbook of Biological Confocal Microscopy. 2nd Edn. Plenum Press, NY.

Rohrbach A (2000) Observing Secretory Granules with a Multiangle Evanescent Wave Microscope. Biophy. J. 78: 2641-2654.

Sako Y; Minoghchi S; Uyemura T (2000) Single-molecule imaging of EGFR signaling on the surface of living cells. Nature Cell. Bio. 2: 168-172.

Sako Y; Yanagida T (2003) Single-molecule visualization in cell biology. *Img. Cell Bio*, pp. SS1-SS5.

Santiago JG; Wereley ST; Meinhart CD; Beebe DJ; Adrian RJ (1998) A particle image velocimetry system for microfluidics. Exp. Fluids 25:316-319.

Shen J; Meng H (1997) A 3D velocity field extraction technique using genetic algorithm. Proc. of The Second International Workshop on PIV-97-Fukui, Japan: 43-50.

Stelzer EHK; Lindek S (1994) Fundamental reduction of the observation volume in far-field light microscopy by detection orthogonal to the illumination axis: confocal theta microscopy. Opt. Commun. 111: 536-547.

Takagi T; Okamoto K (2001), Particle Tracking Velocimetry by Network Model. Proc. of PSFVIP-3, published by CD-Rom

Uemura T; Yamamoto F; Koukawa M (1990) High-speed algorithm for particle tracking velocimetry using binary. J. Vis. Soc. Japan 10-38: 58-64.

Weiss S (2000) Measuring conformational dynamics of bio-molecules by single molecule fluorescence spectroscopy. Nature: Struct Bio7: 724-729.

Xie S (2001) Single-molecule approach to enzymology. Single Molecule 2: 229-236.

Zettner CM ; Yoda M (2003) Particle velocity field measurements in a near-wall flow using evanescent wave illumination. Exp Fluids 34: 115-121.
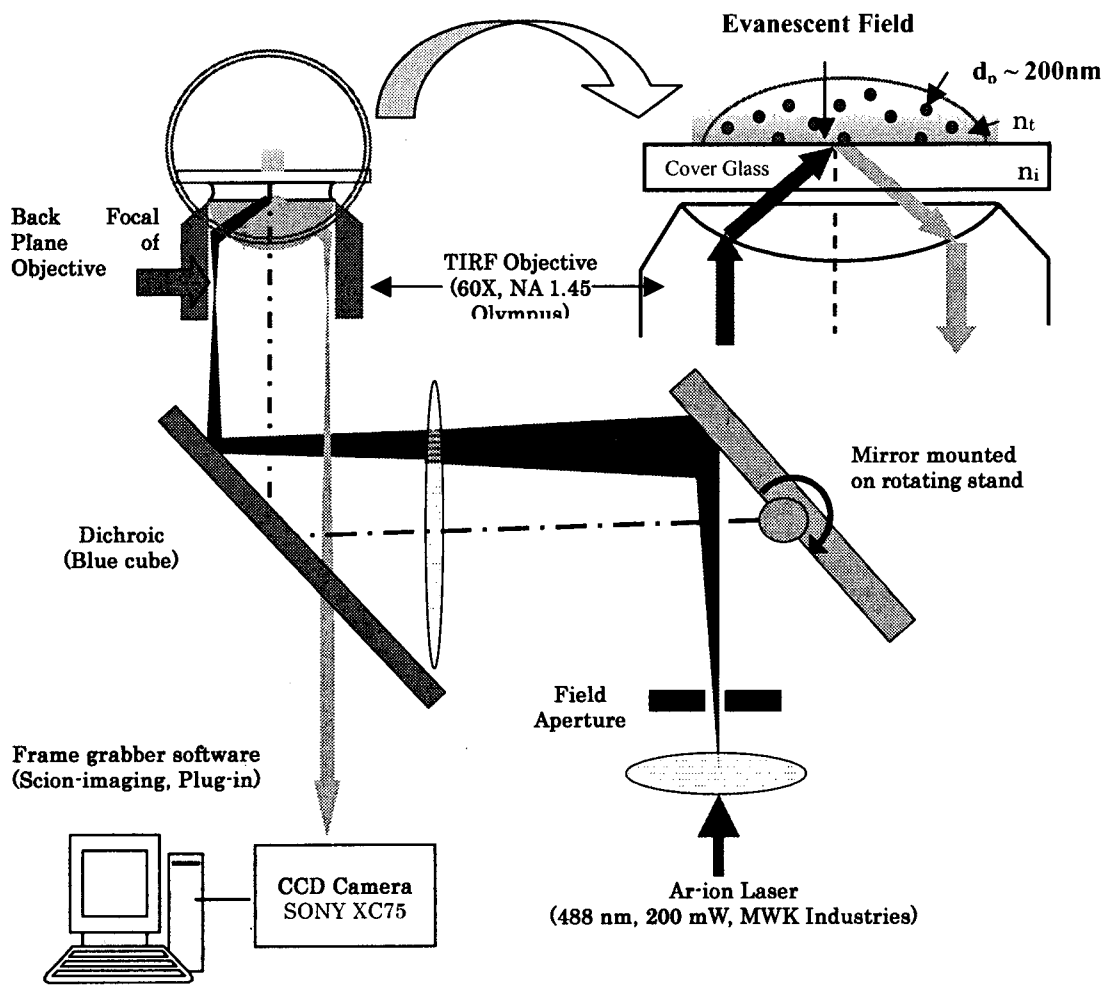
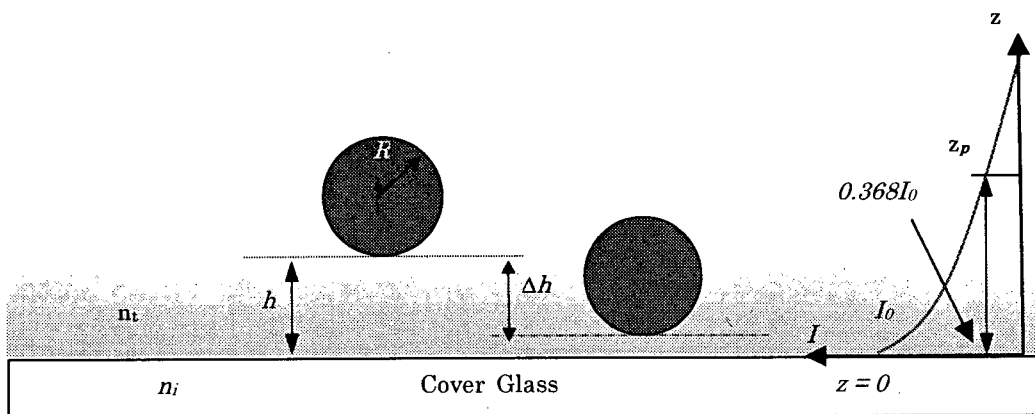Figure 1. TIRFM Experimental set up with High NA Objective Lens.
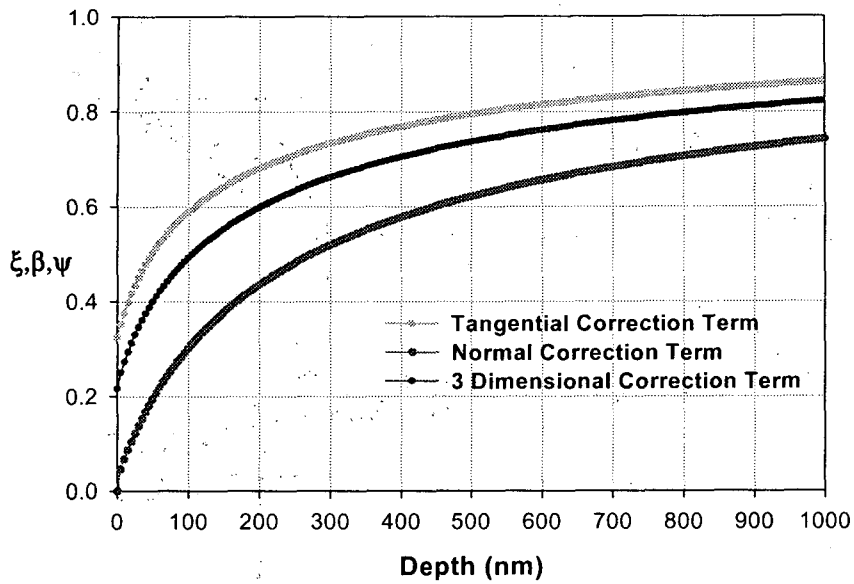

Figure 2. Schematic for Ratiometric Imaging.

Figure 3. Correction Factors for Bulk, Normal and Tangential Diffusion Coefficient as the particle approaches the wall (d_p = 200 nm).
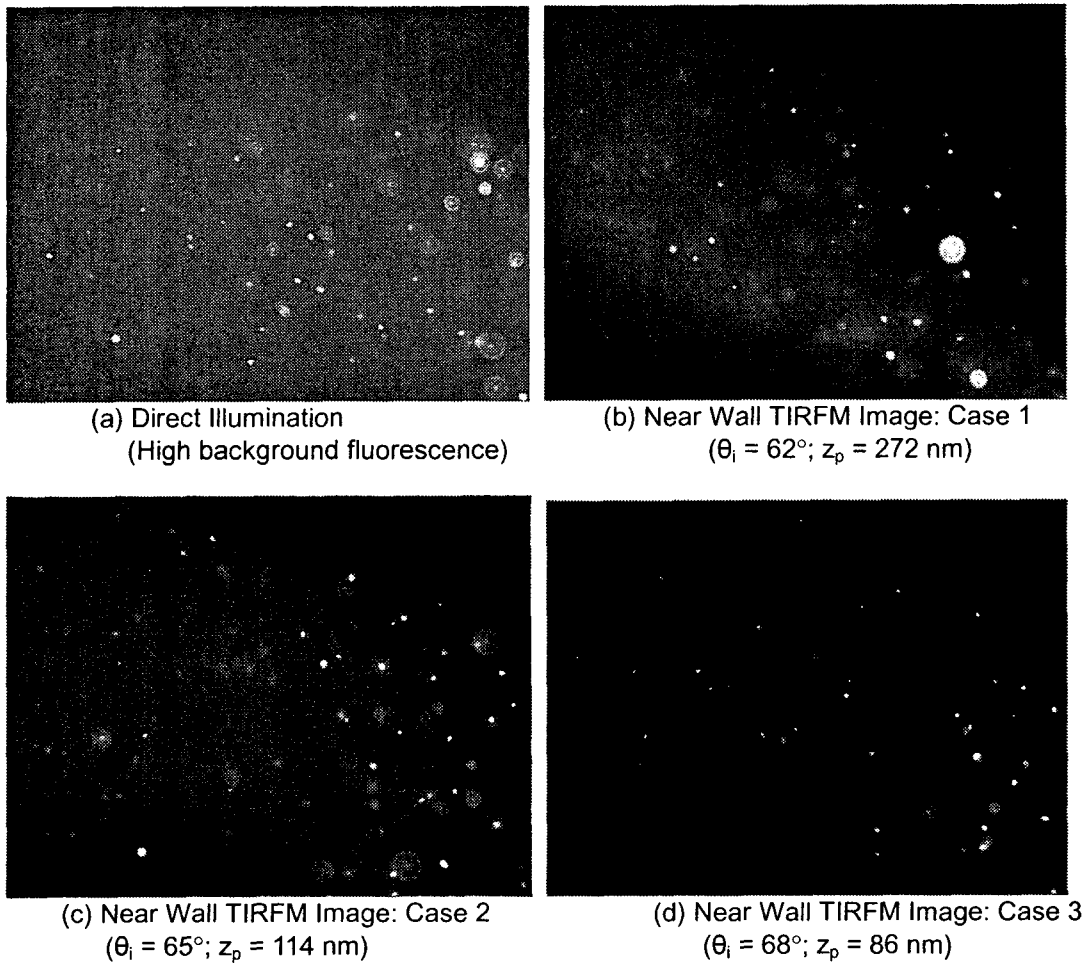

(a) Direct Illumination
(High background fluorescence)

(b) Near Wall TIRFM Image: Case 1
(θ_i = 62°; z_p = 272 nm)

(c) Near Wall TIRFM Image: Case 2
(θ_i = 65°; z_p = 114 nm)

(d) Near Wall TIRFM Image: Case 3
(θ_i = 68°; z_p = 86 nm)

Figure 4. Comparison of direct and evanescent illumination with increasing angle of incidence.
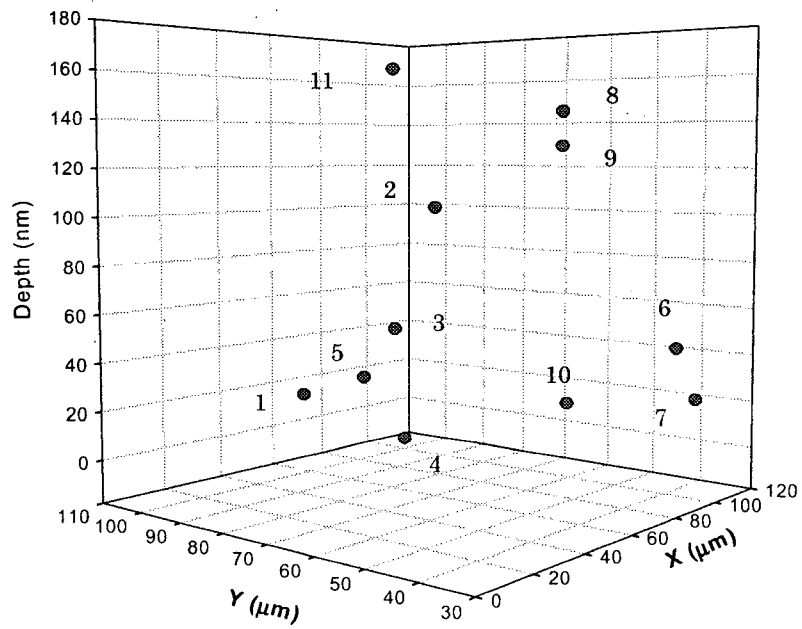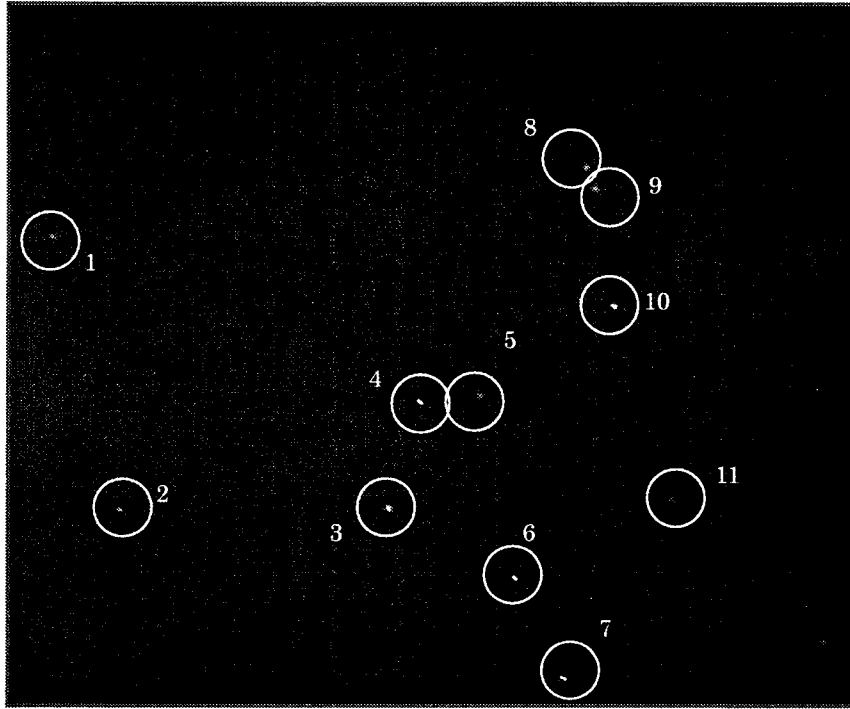
Figure 5. Axial (z) location of Particles for TIRFM Image ($\theta_i = 68°$).
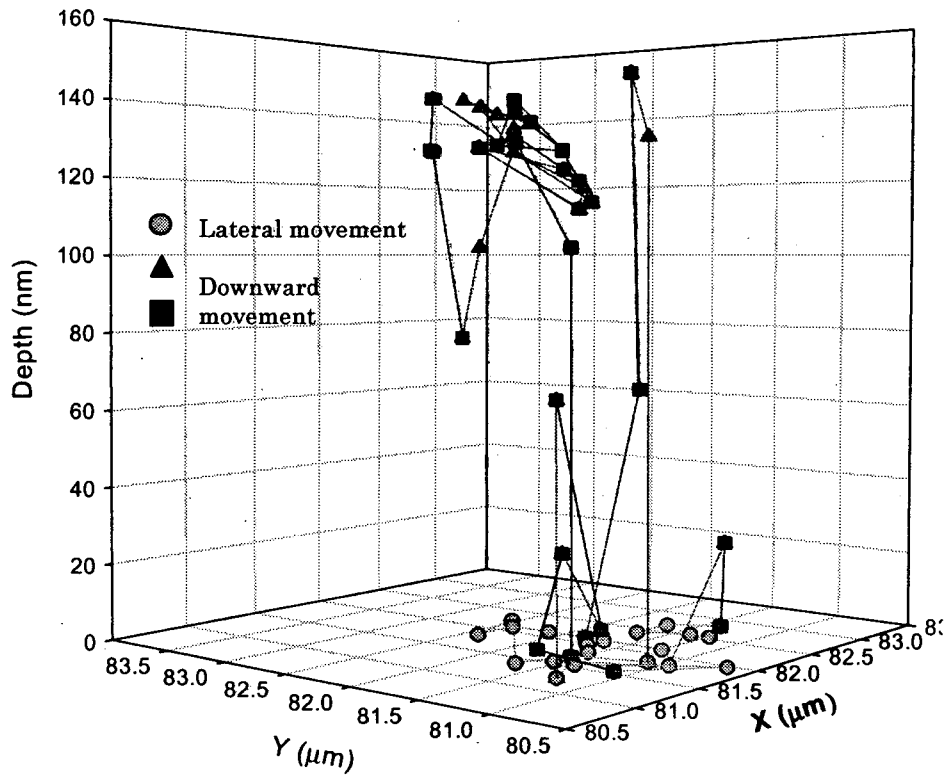
Figure6. 3-D individual particle (#6) tracking of Brownian diffusion (θ_i = 68°).
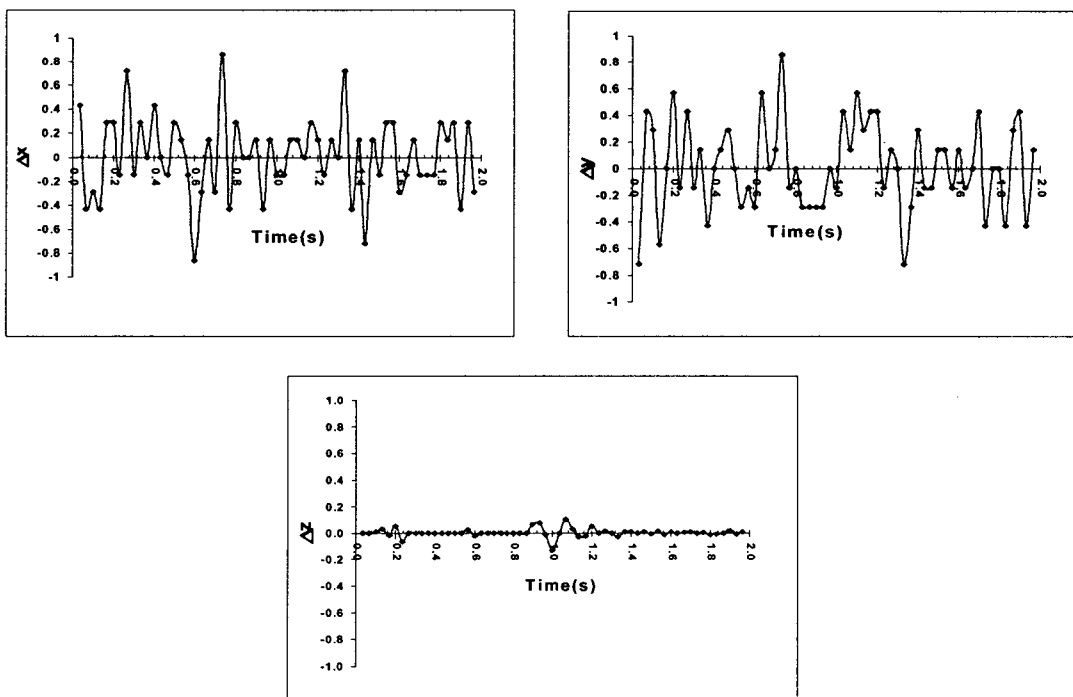
Figure 7. 3 dimensional displacements of particle(#6) tracked over 59 frames.
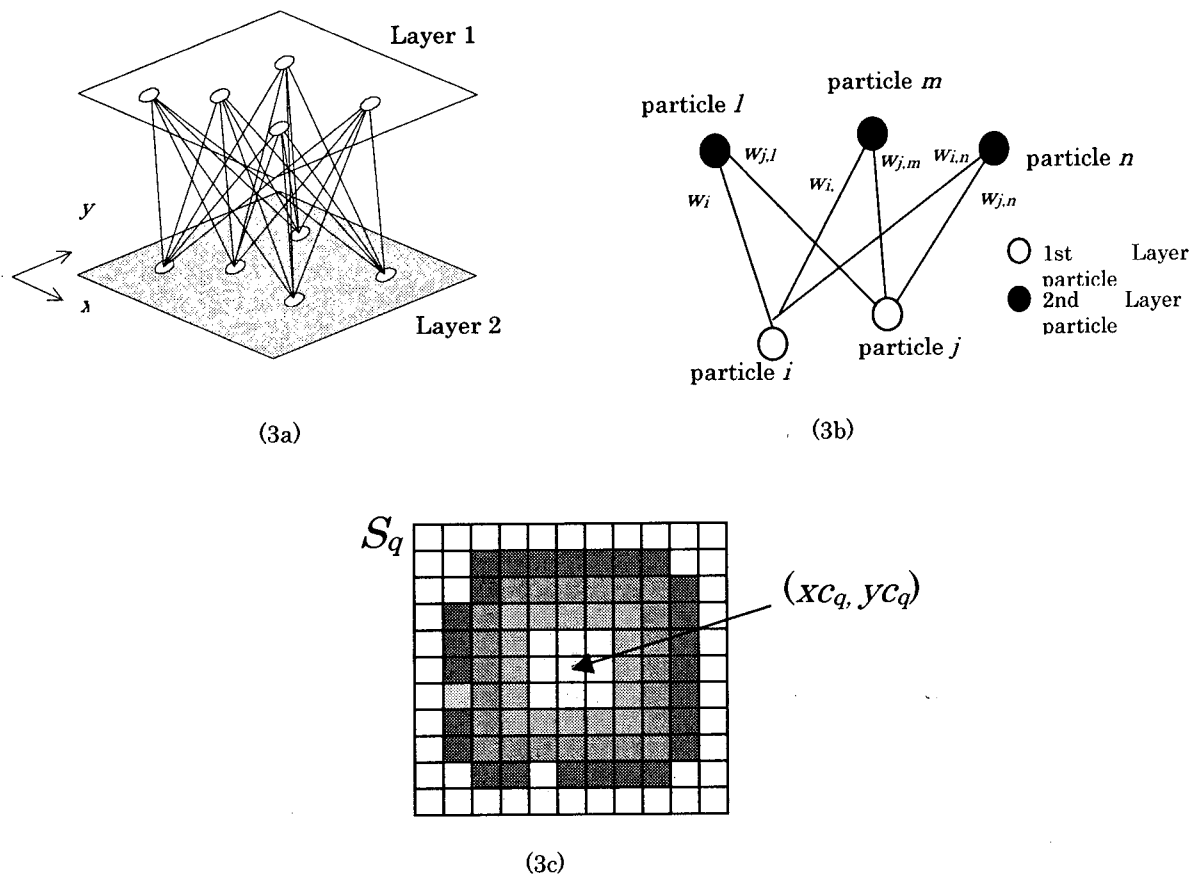
Figure 8. (a)Architecture of the network model; (b) Particle identification for layers; (c) Sample particle center with label q.
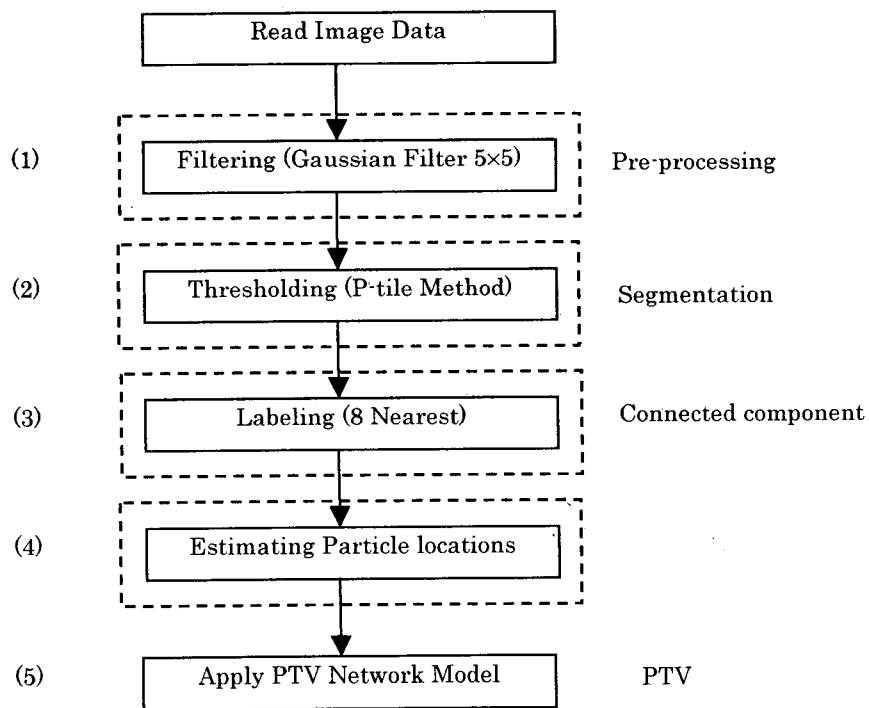

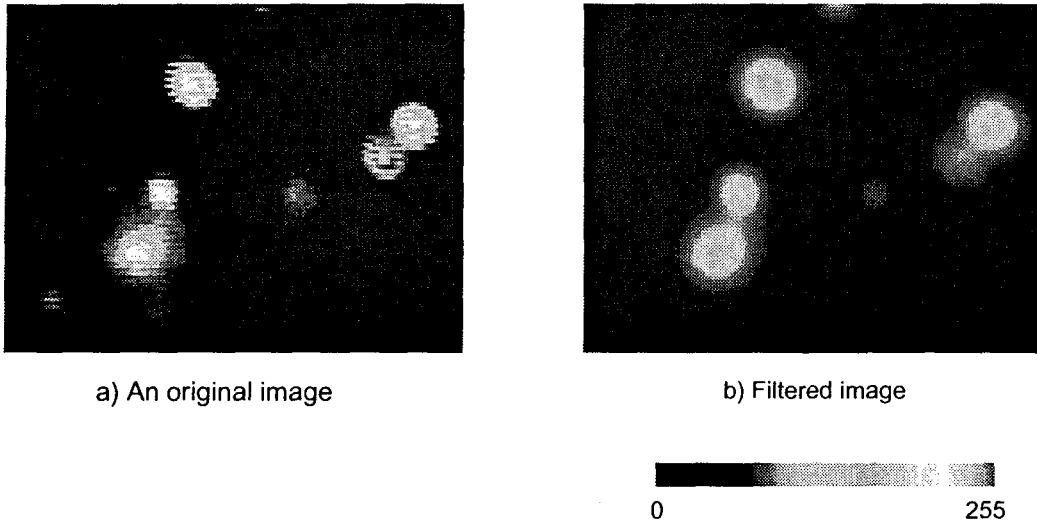Figure 9. Overview of the Image processing procedure.

a) An original image

b) Filtered image

0   255

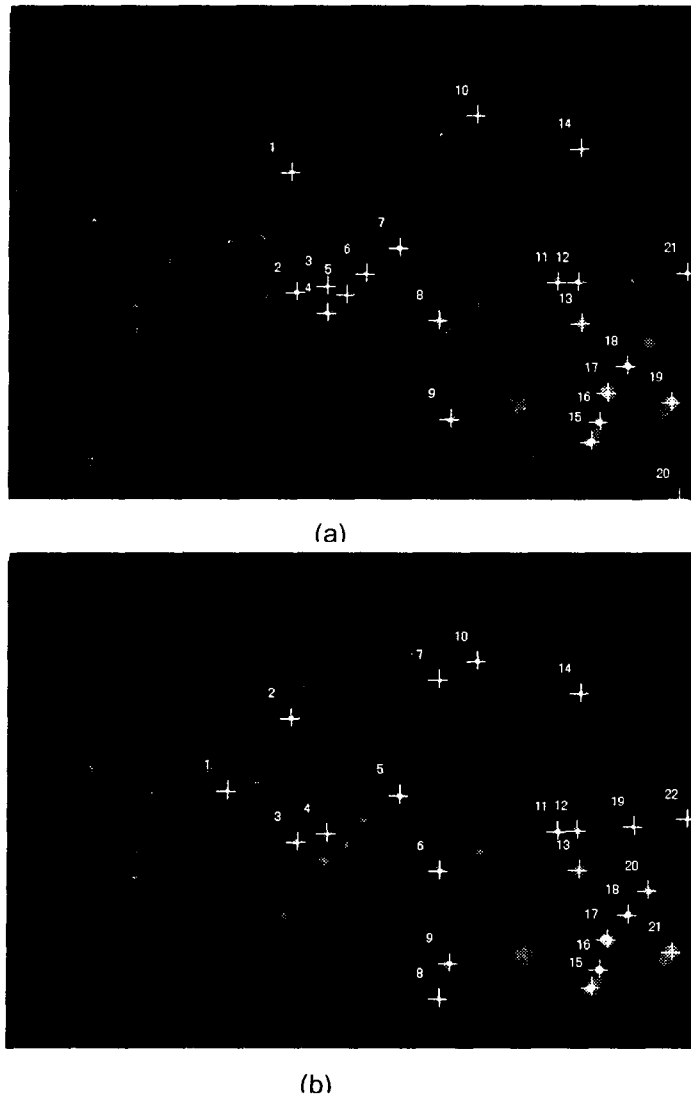Figure 10. Noise reduction by 5×5 Gaussian Filtering

(a)

(b)

Figure 11. Determination of particle centers. Detected particles are labeled by the number. Crosses are the center of the particle.
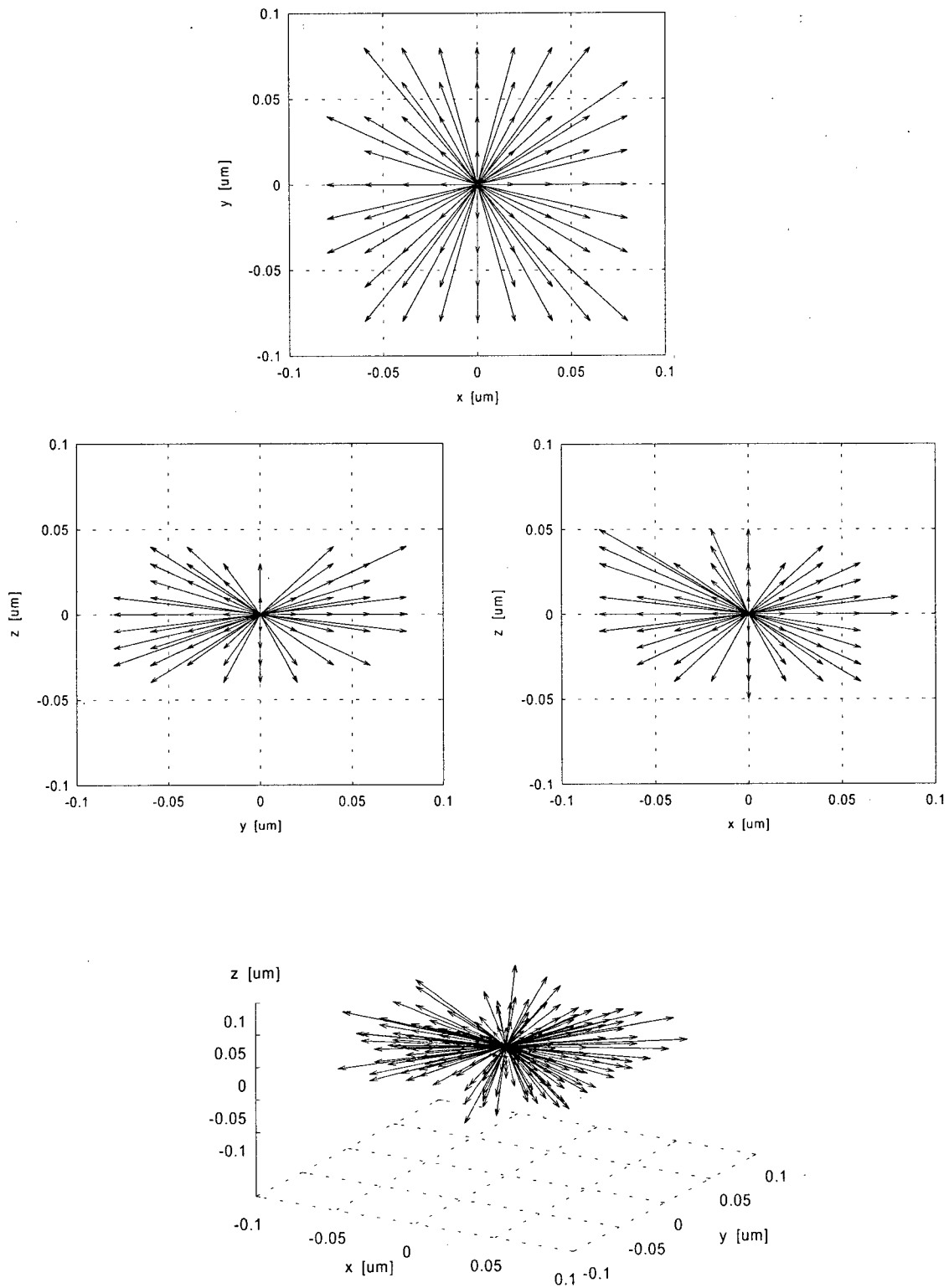
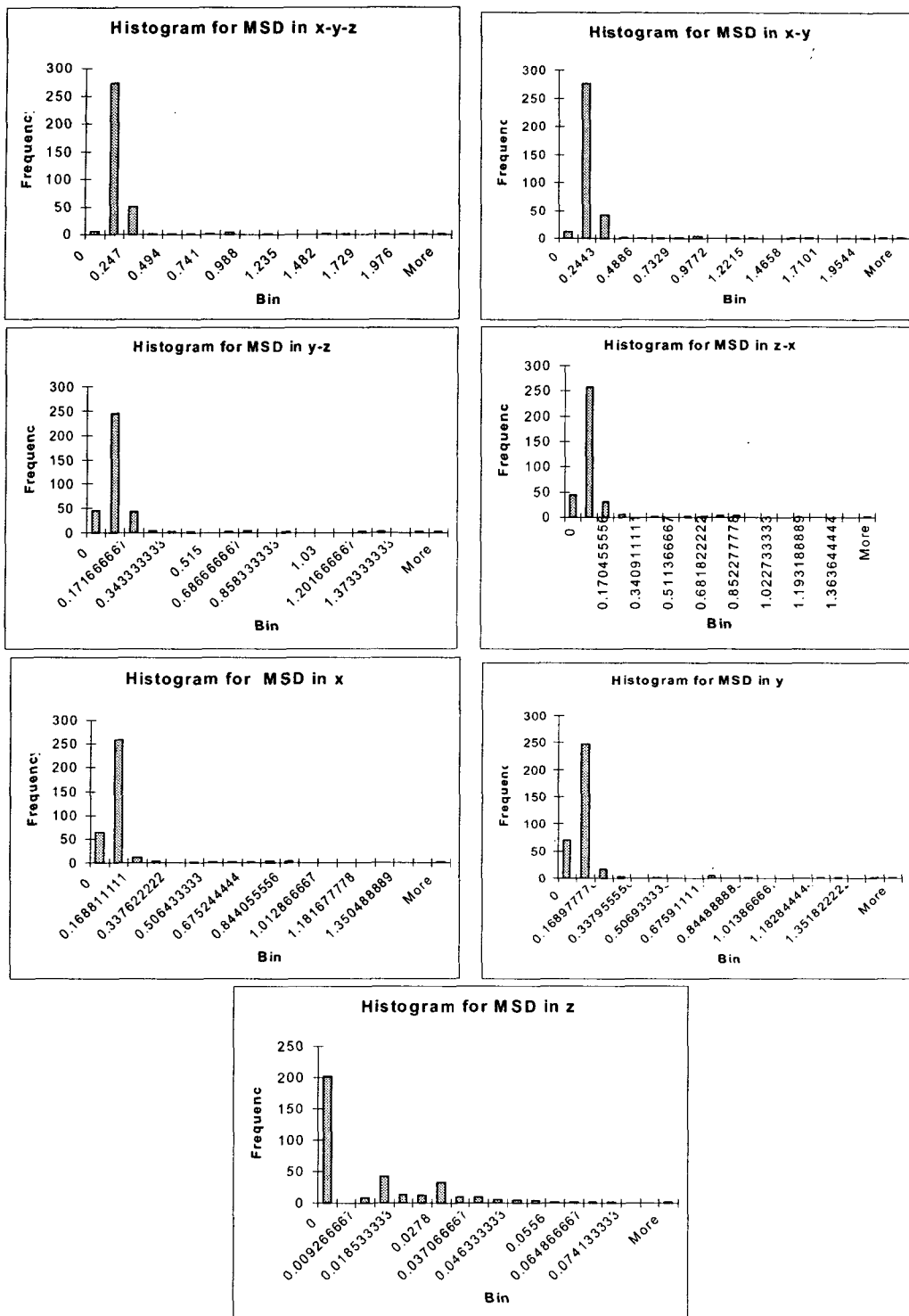Figure 12. Plots of Displacement in x-y, x-z, y-z and x-y-z directions.

Figure 13. Histograms for Mean Square Displacements in different directions.

Table 1. Comparison of Theoretical and Experimental Mean Square Displacement values

Parameter	Units	Theory	Neural Network Based PTV	5 particle Manual Tracking
$< r >^2$	μm^2	0.1995	0.1885	0.201 ± 0.047
$< x >^2$		0.0804	0.0857	0.102 ± 0.023
$< y >^2$		0.0804	0.1017	0.0974 ± 0.023
$< z >^2$		0.0387	0.0011	0.003 ± 0.001